PCCP

Reaction-driven Selective CO2 Hydrogenation to Formic Acid on Pd(111)

Journal:	*Physical Chemistry Chemical Physics*
Manuscript ID	CP-ART-04-2022-001971.R1
Article Type:	Paper
Date Submitted by the Author:	03-Jun-2022
Complete List of Authors:	Zhang, Hong; Stony Brook University, Chemistry Wang, Xuelong; Brookhaven National Laboratory, Chemsitry Liu, Ping; Brookhaven National Lab, Chemistry

ARTICLE

Reaction-driven Selective CO_2 Hydrogenation to Formic Acid on Pd(111)

Received 00th January 20xx,
Accepted 00th January 20xx

DOI: 10.1039/x0xx00000x

Hong Zhang,[a] Xuelong Wang,[b] and Ping Liu[a,b,*]

Converting CO_2 to useful fuels and chemicals has gained great attention in the past decades, yet the challenge persists due to the inert nature of CO_2 and the wide spread of products formed. Pd-based catalysts are extensively studied to facilitate CO_2 hydrogenation to methanol via reverse water gas shift (rWGS) pathway or formate pathway where formic acid may serve as an intermediate species. Here, we report the selective production of formic acid on the stable Pd(111) surface phase under CO_2 hydrogenation conditions, which is Pd(111) fully covered by chemisorbed hydrogen, by combining Density Functional Theory (DFT) and Kinetic Monte Carlo (KMC) simulation. The results show that with the full coverage of hydrogen, instead of producing methanol as reported for Pd(111) the CO_2 activation, is highly selective to formic acid via a multi-step process involving the carboxyl intermediate. The high formic acid selectivity is associated with surface hydrogen species on Pd(111), which not only acts as hydrogen reservoir to facilitate the hydrogenation steps, but also enables the formation of confined vacancy sites to facilitate the production and removal of formic acid. Our study highlights the importance of reactive environments, which can transform the surface structures and thus the activity/selectivity of catalysts.

1. Introduction

Catalytic conversion of CO_2 into value adding chemicals is a promising approach that has attracted great interest in past decades. The progress has been made on CO_2 fixation through thermal catalysis, electrocatalysis, photocatalysis, biochemical and chemo-enzymatic catalysis.[1, 2] Common products from CO_2 conversion include methanol,[3-9] ethanol,[10] syngas, [11-14] formic acid,[15, 16] and methane.[17, 18] Pd has been extensively reported to catalyze the CO_2 conversion in various routines via the form of supported nanoscale Pd structures or Pd based alloys benefited from its ability to activate H_2. [19-25] Melian-Cabrera et al. reported the effect of Pd incorporation on CO_2 hydrogenation over the CuO-ZnO catalysts. The synergy between Pd atoms on active Cu sites was proposed, where the promoted H_2 adsorption by Pd atom increased the spillover of *H adatoms to metallic oxide support, thus further enhanced the methanol yield.[26] The Pd-support synergy was also demonstrated by Rui et al. for In_2O_3 supported Pd nanoparticles, where Pd helped hydrogen dissociation on the dominantly exposed (111) facets and thus generation of oxygen vacancy to facilitate the CO_2 activation and conversion to methanol on In_2O_3.[24] Besides, according to the recent study by Zhang et al. the basicity of TiO_2 or CeO_2 support and the electronic structure of Pd nanoparticles could determine the catalytic behaviors during CO_2 hydrogenation to formic acid.[16] Nevertheless, so far there is no generally accepted mechanism to illustrate how Pd-based catalysts behave under the reaction conditions.

To address the roles that Pd sites play during the CO_2 hydrogenation at a molecular level, theoretical studies were performed based the extended Pd surfaces or small Pd clusters.[27-30] The results show that the activation of $*CO_2$ on the Pd sites alone undergoes via formate (*HCOO) and carboxyl (*HOCO) intermediates (Figure 1). Both intermediates can lead to formation of formic acid (HCOOH), which breaks down to *HCO and *OH and is finally hydrogenated to methanol (CH_3OH). However, the previous theoretical models used to describe Pd have not considered the possible effect from the reactive chemical environments of CO_2 hydrogenation. Indeed, under the CO_2 electroreduction the phase transformation from pure Pd to α- or β-PdH depending on the conditions was observed, which determined the catalytic activity and selectivity.[31, 32] Given that, to gain accurate insights of CO_2 hydrogenation mechanism on Pd, it is crucial to determine the stable surface phase of Pd under reactive conditions.

Here, the combined density functional theory (DFT) calculations and kinetic Monte Carlo (KMC) simulations were performed to study the behaviors of Pd(111) during the CO_2 hydrogenation. Our study was built on our recent work, which mapped the surface diagram of Pd(111) with exposure to H_2 and CO_2 under different temperatures and various pressures.[33] By combining Ambient Pressure X-ray Photoelectron Spectroscopy and DFT simulations, we investigated the surface species under varying experimental conditions. The DFT calculations predicted multiple surface phases ranging from bare Pd(111) to Pd(111) partially (coverage: 0.25 ML, 0.5 ML and 0.75 ML)/fully (coverage: 1ML and

[a] Department of Chemistry, Stony Brook University, Stony Brook, NY 11794, USA
[b] Chemistry Division, Brookhaven National Lab, Upton, NY 11973, USA
* Corresponding author: pingliu3@bnl.gov (P. L.)
Electronic Supplementary Information (ESI) available: [details of any supplementary information available should be included here]. See DOI: 10.1039/x0xx00000x

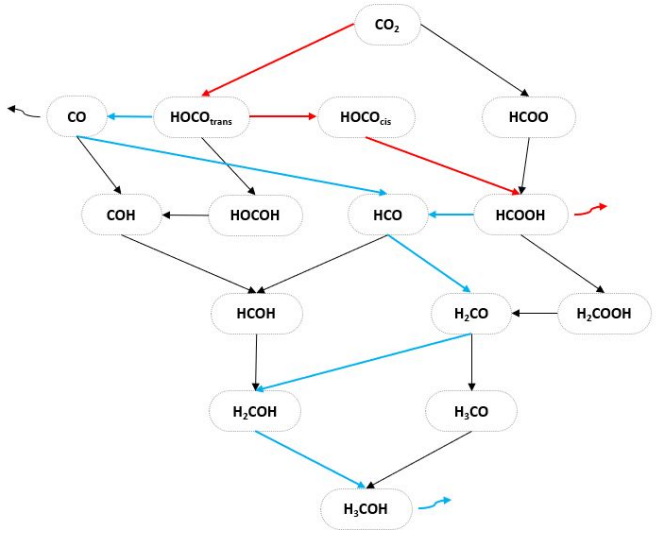

Figure 1. Reaction steps considered for methanol synthesis from CO_2, the preferred pathways are highlighted in blue for Pd(111) according to the previous study[27, 28] and red for $*H_{1ML}$/Pd(111) according to the present study. [curved arrow: product desorption]

1.25 ML) covered by chemisorbed hydrogen and partially covered by *CO and/or *O, as well as hydride PdH(111) and oxide PdO(111) surfaces depending on their formation energy under the temperature and partial pressure of CO_2/H_2. Under the typical CO_2 hydrogenation conditions (500K, ~10^4 Torr of CO_2/H_2), the Pd(111) covered by 1 ML of *H or $*H_{1ML}$/Pd(111) in our notation (Figure S1) was found to be the most stable surface phase. Given that, the current study selected $*H_{1ML}$/Pd(111) as the model surface to describe the catalytic CO_2 hydrogenation on Pd(111). The results show that $*H_{1ML}$/Pd(111) behaves differently from Pd(111) [27, 28], being able to selectively stabilize the *HOCO intermediate and promote the HCOOH production. The highly enhanced HCOOH selectivity is not only benefited from the persist *H reservoir, but also the confined *H vacancy sites that are generated during the reaction and active for selective HCOOH production. Our study highlights the important dependence of surface phase and thus catalytic activity/selectivity on the reactive chemical environments, which can be considered as an alternative way to tune catalytic behaviors.

2. Computational Methods

To study the CO_2 hydrogenation on $*H_{1ML}$/Pd(111) surface, spin polarized DFT calculations were carried out with the Vienna Ab initio Simulation Package (VASP).[34-36] The Perdew-Burke-Ernzerhof (PBE)[37] functional was employed to describe electronic exchange and correlation, pseudopotential files used were those prepared by Vaspkit.[38] Note that the vdW interaction was not included which showed limited effects on the trends in the adsorption energy of different adsorbates according to the previous study,[39] and thus the selectivity of CO_2 hydrogenation which is the focus of current study. The system is represented by a 5×5 slab unit of Pd(111) surface based on a DFT optimized 3.952Å face center cubic (FCC) Pd Fm3m unit cell (Figure S1), the slab consist of four layers of Pd atoms, and covered with 1ML of chemisorbed *H at $Pd_{3\text{-}fcc}$ sites. The unit is extended to infinite surface in periodic condition and 20Å vacuum is placed above the surface to ensure a minimum of 15Å of space when intermediate molecules are adsorbed, and dipole correction along the direction of vacuum is included. The bottom two layers of the surface is frozen to represent the bulk structure underneath, the top two layers along with *H atoms and adsorbed species are allowed for relaxation. Atomic optimizations were initialized using the Conjugate Gradient ionic relaxation algorithm[40] then converged with the RMM-DIIS ionic relaxation algorithm[41] with a plane wave cutoff energy of 400eV. A 3×3×1 Monkhorst-Pack grid and first order Methfessel -Paxton with smearing width of 0.2eV were used to integrate over Brillouin zone. An electronic convergence level of 1×10^{-6} eV was employed to obtain convergence of the electronic structure, and ionic relaxation was activated and satisfied until the Hellman-Feynman force was less than 0.02 eV/Å on each ion. The energy of absorption B.E.(adsorbate) was determined by the energy difference between surface with adsorbate and the sum of initial surface and gas phase molecule. As the initial surface is covered by *H, the reference energy for all intermediate species is aligned with the free energy of gas phase CO_2 molecule.

The search of transition states was conducted by climbing image nudged elastic band (NEB) method[42-45], four equal distanced intermediate images were generated by linear interpolations between optimized initial and final configuration for each reaction step. The optimization is initiated with Faster Internal Relaxation Engine (FIRE) [46] algorithm and stopped when the force-based RMM-DIIS algorithms[47] reaches 0.05 eV/Å on each ion. Saddle points were confirmed by vibrational frequency calculation that only applies to intermediate molecule and surface atoms that directly interacted with the adsorbate, other atoms in the system were frozen. In each elementary step of the reactions, each consumed surface *H is assumed to be filled immediately once the vacancy is not occupied because the phase diagram confirmed a wide range of H_2 partial pressure that preferably covers Pd(111) with 1ML of atomic H.[33]

The reaction barriers (E_a) were implemented to a 2×2 $*H_{1ML}$/Pd(111) unit cell for Kinetic Monte Carlo (KMC) simulation (Figure S2). All possible forward and reverse elementary steps obtained from DFT calculations were included, except the re-adsorption of gas phase product molecules. The unit cell is sampled on a 32×32 matrix and the Eley-Rideal (ER) reaction of gas phase CO_2 hydrogenation to *HOCO is considered as the first step of all pathways. The rate constant of CO_2 activation was calculated according to transition state theory:[48]

$$R_{(T,P)} = \frac{k_B T}{h} \exp\left(-\frac{(\Delta G^{TS}_{(T,P)} - ^{IS})}{k_B T}\right)$$

R is the reaction rate, k_B stands for Boltzmann constant, T is the temperature in kelvin, h is the Planck constant. The total free energy of the gas phase CO_2 initial state (IS) is calculated as $G_{IS} = E^0 + ZPE - TS + \Delta H_{(T)} + k_B T \ln(P/P_0)$, where the total energy of gas molecule E^0 is calculated from DFT, zero point energy (ZPE) and entropic term TS is obtained from the NIST Computational Chemistry Comparison

and Benchmark Database (CCCBDB)[49] at the same level of theory used in our calculations, the enthalpy change $\Delta H_{(T)}$ at temperature T is obtained from the NIST-JANAF thermodynamic table,[50] and the CO_2 partial pressure dependent term is calculated as a reference P_0 = 1 bar (Table S1). The total free energy of transition state on surface is calculated $G_{TS} = E^0 + ZPE - TS$, so as in the following surface reaction rates. And the entropy S and ZPE of surface species are calculated from the vibrational modes ν_i:

$$S = k_B \sum_i \left[\frac{\frac{h\nu_i}{k_B T}}{exp(\frac{h\nu_i}{k_B T}) - 1} - ln(1 - exp(-\frac{h\nu_i}{k_B T})) \right]$$

$$ZPE = \frac{1}{2} \sum_i h\nu_i$$

The lateral interaction is approximated by limiting the CO_2 coverage below 0.25monolayer (ML) due to the focus of this work is the selectivity but not to compare the exact activity with experimental settings. The selectivity is compared with the KMC calculated turn-over-frequency (TOF) of the product molecules, which is the number of molecules released per active site per second:

$$TOF(\mathrm{x}) = \frac{\text{Number of molecule(x) produced}}{\text{Number of Active site} \cdot \text{Simulation time}}$$

$$Selectivity(\mathrm{x}) = \frac{\mathrm{TOF(x)}}{\mathrm{TOF(all\ product)}}$$

3. Result and Discussion

3.1 DFT study

Different from the case of plain Pd(111) surface,[27, 28] CO_2 does not interact well with $*H_{1ML}$/Pd(111). Instead, CO_2 is weakly adsorbed via O-H electrostatic interaction with the binding energy of -0.02 eV and the molecule remains in the linear O=C=O conformation (Figure 2). For the first hydrogenation step CO_2 approaches to the surface and picks up a *H atom via O-H bond association to form monodentate *HOCO intermediate via a trans motif, $*HOCO_{trans}$ (Figure S3a). The removal of *H due to the hydrogenation generates an isolated or surface hydrogen vacancy site, or Hv in our notation, which is confined by the surrounding *H atoms, enabling the anchor of $*HOCO_{trans}$ on the Pd_{top} site via the C atom. In addition, the -OH group of $*HOCO_{trans}$ points down towards Hv (Figure 2). This is an endothermic step with reaction energy (ΔE) of 0.78eV and activation barrier (E_a) of 1.40eV (Figure 3). By contrast, the formation of *HCOO via the C-H bond association at the Hv site (Figure S3b) is less favorable thermodynamically (ΔE = 1.12 eV) and kinetically (E_a= 1.83eV), and is not feasible under the reaction conditions according to the KMC simulations shown below.

The significant preference to *HOCO over *HCOO is rarely observed on metal-based catalysts. On Pd(111), the reaction energy for CO_2 hydrogenation to *HOCO and *HCOO is comparable (ΔE= 0.43eV for *HOCO and ΔE= 0.46eV for *HCOO) (Figure S4), which agrees well with previous studies.[27, 28] Upon going from Pd(111) to $*H_{1ML}$/Pd(111), $*HOCO_{trans}$ is destabilized by 0.35eV to 0.78eV on $*H_{1ML}$/Pd(111), while *HCOO is destabilized by 0.66eV to 1.12eV. Such selective destabilization of *HCOO over *HOCO is associated with the confined single Hv site. It hinders the binding of *HCOO, which requires two sites, more significantly than that of $*HOCO_{trans}$, which requires one site. This is also evidenced by the extended bond length between adsorbate molecules to the surface. On Pd(111), the C-Pd bond of $*HOCO_{trans}$ is 1.98Å, and is stretched to 2.05Å on $*H_{1ML}$/Pd(111). A larger elongation is observed for *HCOO, where the O-Pd bond length is increased from 2.13Å to 2.24Å.

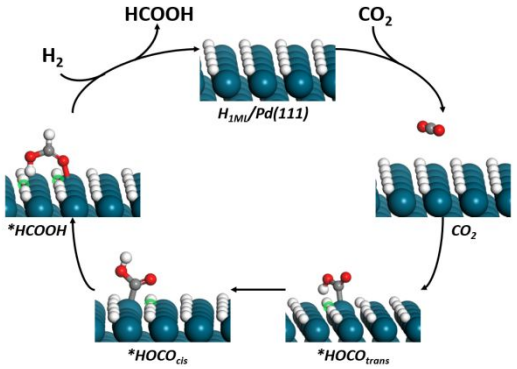

Figure 2. Key intermediates in the formic acid pathway reaction cycle on $*H_{1ML}$/Pd(111). [Blue: Pt; White: H; Grey: C; Red: O; Green: Hydrogen vacancy]

There are three possibilities for the formed $*HOCO_{trans}$: hydrogenating the carbon site to form *HCOOH via the HCOOH pathway, hydrogenating the terminal oxygen to form *HOCOH via the HOCOH pathway, and cleaving the C-O bond to form *CO via the reverse water gas shift (rWGS) pathway. The formation of *HCOOH from $*HOCO_{trans}$ likely undergoes the transformation to $*HOCO_{cis}$ first with the -OH group flipped upward and the terminal -O tilted toward surface (ΔE = 0.13 eV, E_a = 0.78eV, Figures 2c, 3 and S3c). The tilted configuration of $*HOCO_{cis}$ lowers the position of C atom closely to the surface *H species, so that the hydrogenation via the C-H bond association can occur easily (ΔE = -0.34 eV, E_a = 0.53eV, Figure S3d). Upon the formation of C-H bond, the Pd-C bond breaks, and Pd-O bond forms simultaneously, which is followed by the rotation of -CH group outward the surface and -OH group pointed downward to the surface as seen for $*HOCO_{trans}$ (Figure 2). Similar transition mechanism was also identified by Brix et al.[27] and Scaranto et al.[51] on Pd(111). However, the stability of produced *HCOOH is different. The decomposition of *HCOOH to *HCO and *OH was observed for Pd(111), which led to the production of methanol. On $*H_{1ML}$/Pd(111) surface, the *HCOOH dissociation is hindered by the surface *H species, which limits the number of Pd sites available for the dissociation. As a result, the reaction energy is over 2eV due to significant lateral repulsion associated with the co-adsorption of dissociated *HCO and *OH fragments. By comparison, the release of *HCOOH into the gas form is more favorable, which is slightly endothermic by 0.18eV (Figure 3). Finally, the catalytic cycle will be

closed by facile hydrogenation dissociation to refill of the Hv site on $*H_{1ML}$/Pd(111) (Figure 3).

The formed $*HOCO_{trans}$ from CO_2 hydrogenation also points the terminal -O atom downward the surface to enable the hydrogenation via O-H bond association and the formation of *HOCOH species with both -OH groups pointed downwards (Figure S3e). In term of energetics (ΔE = 0.30 eV, E_a = 0.96eV), the HOCOH pathway is less favorable than that of the HCOOH pathway (Figure 3). In addition, the further dissociation to *COH and *OH is very difficult (ΔE = 1.65 eV, E_a = 2.02eV, Figure S3f), which is again associated with the limited Pd sites and thus unstable dissociated states as seen for *HCOOH dissociation. According to the KMC results shown below, the formed *HOCOH likely transforms back to $*HOCO_{trans}$ under the reaction conditions.

Similar site-limitation and hindered dissociation at the confined Hv sites were also observed for the dissociation of $*HOCO_{trans}$ to *CO and *OH via the rWGS pathway, which is the least favorable among three pathways studied (ΔE = 0.96eV, E_a = 1.19eV, Figure 3). In this case, the dissociated *CO and *OH fragments share the same Pd hollow site generated by hydrogenation (Figure S3g), resulting in the high endothermicity and barrier. The further hydrogenation forms water from *OH (ΔE = -0.94eV, E_a = 0.63eV, Figure S3h), where water is physiosorbed for a facile desorption. While the desorption of *CO requires 1.56eV of activation energy, considering the entropic contribution along with the ZPE correction, the energy cost can be lowered to 1.02eV at 300K, and 0.77eV at 500K. Alternatively, *CO can undergo further hydrogenation to either *COH (ΔE = 0.99eV, E_a = 1.56eV, Figure S3i) or *HCO (ΔE = 1.27eV, E_a = 1.84eV, Figure S3j). Considering much higher activation barriers compared to desorption of *CO, the further hydrogenation of *CO to methanol as seen for Pd(111) [27] is not likely to occur on $*H_{1ML}$/Pd(111).

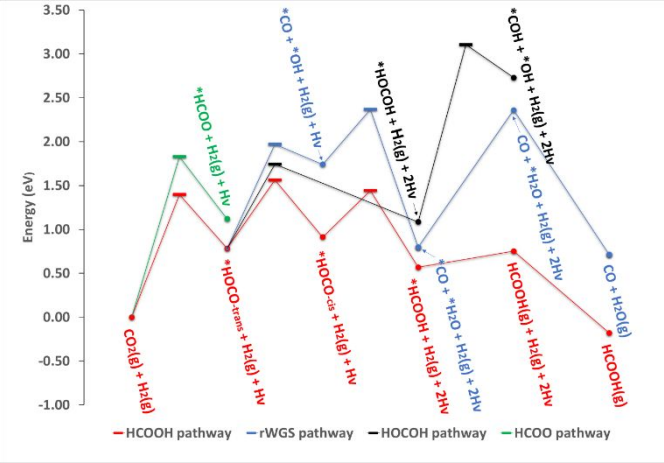

Figure 3. Reaction diagram of CO_2 hydrogenation pathways on $*H_{1ML}$/Pd(111). (• intermediates; ━ transition states; *adsorbed species; Hv: Hydrogen vacancies;)

Overall, according to the previous study of Pd(111),[27, 28] kinetically the Langmuir-Hinshelwood (LH) mechanism is observed for the initial CO_2 hydrogenation. It starts with strongly chemisorbed $*CO_2$ and favors the formation of *HOCO or *HCOO species by hydrogenation of the oxygen or carbon atom, which eventually leads to methanol production. Due to the fully covered by *H on $*H_{1ML}$/Pd(111), the first hydrogenation step is likely to follow the Eley–Rideal (ER) mechanism, and the rest hydrogenation of CO_2 seem to proceed only via the O-H bond association, which likely enables HCOOH formation via *HOCO intermediate (Figure 2). To confirm the hypothesis based on DFT calculations, the KMC simulation was performed based on the energies calculated using DFT.

3.2 KMC Simulations

To gain better understanding of reaction kinetics of CO_2 hydrogenation on the $*H_{1ML}$/ Pd(111) surface, the DFT-calculated energies (Figure 3) of the different pathways based on $*HOCO_{trans}$ intermediate were used to estimate the reaction rates using KMC simulations. Here, we excluded the formate pathway due to the obvious preference of $*HOCO_{trans}$ over *HCOO according to the DFT calculations. Such reaction network can lead to the productions of HCOOH along the HCOOH pathway and/or CO/water along the rWGS pathway. At 500K and under CO_2 partial pressure of 1 bar, the reaction barely occurs, and only trace amount of HCOOH and no CO/water is observed (Table S2), due to the limitation to overcome the barrier of 1.40 eV for the initial CO_2 hydrogenation (Figure 3). In fact, the CO_2 hydrogenation to *HOCO is the conversion-controlling step for CO_2 hydrogenation on $*H_{1ML}$/ Pd(111). To facilitate the CO_2 conversion, the reaction temperature and the CO_2 partial pressure

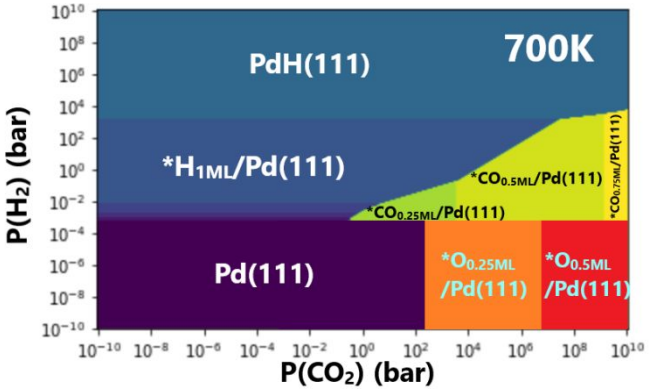

Figure 4. Pd(111) phase diagram at 700K depending on the partial pressures of CO_2 and H_2. The phases between Pd(111) and $*H_{1ML}$/Pd(111) corresponded to the Pd(111) surfaces with gradually incremental coverage of *H.

was increased up to 700 K and 100 bar, respectively. Here, we note that to ensure the stability of surface under the elevated temperatures, the surface diagram of Pd(111) under the CO_2 hydrogenation conditions was calculated at 700K by following the same protocol described in previous work.[33] The results show that the $*H_{1ML}$/ Pd(111) surface remains as stable between 6.8×10^{-3} ~ 1.3×10^{3} bar of H_2 at 700K (Figure 5a) with moderate CO_2 partial pressures, which is commonly achievable in CO_2 hydrogenation experimental settings.[52]

By raising the temperature from 500K to 700K under the CO_2 pressure of 1 bar, the production of HCOOH grows exponentially, which emerges at 600 K with TOF of 54.7 molecules·s^{-1}·$site^{-1}$ and significantly increases at the temperature higher than 650 K with TOF of 754.1 molecules·s^{-1}·$site^{-1}$ (Figure 5a); while the produced CO/water remains as very small mount. Similar promotion on HCOOH production rather than CO/water was also observed by increasing the partial pressure of CO_2 at 500 K (Figure 5b). The difference is that the pressure-dependent promotion shows a linear-like trend and the variation in TOF of HCOOH is less sensitive to pressure than that to temperature (TOF =0.1 at 1bar, TOF =8.1 at 100 bar). At 700K and under CO_2 partial pressure of 10 bar, the selectivity to HCOOH can be reached to 99.97% (Table S2).

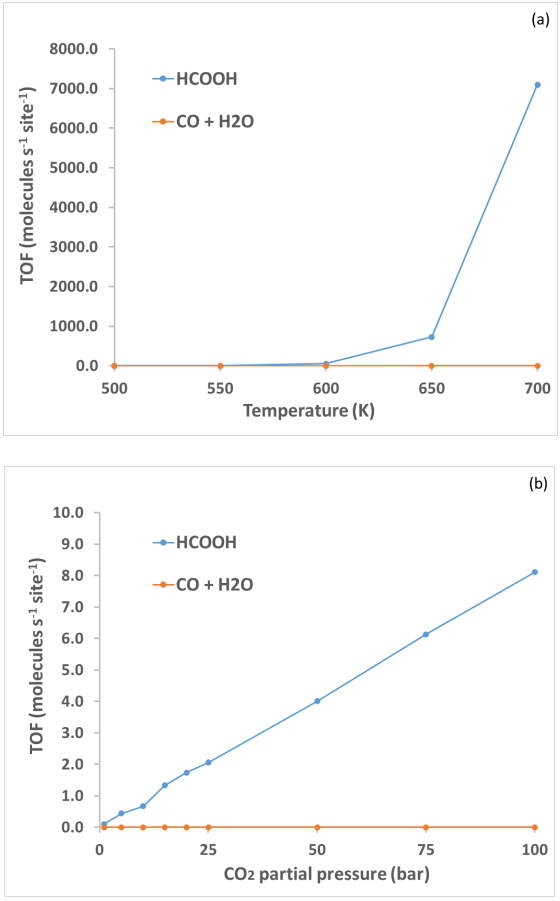

Figure 5. KMC-estimated variation in TOF with (a)the temperature for CO_2 hydrogenation on the $*H_{1ML}$/ Pd(111) surface with the CO_2 partial pressure of 1 bar . (b)the partial pressure of CO_2 for CO_2 hydrogenation on the $*H_{1ML}$/Pd(111) surface at 500K.

The selectivity of CO_2 hydrogenation on $*H_{1ML}$/Pd(111) depends on the competition in conversion of *HOCO via the three pathways. The KMC-estimated high HCOOH selectivity is benefited from the preferential *HOCO hydrogenation to *HCOOH (E_a = 0.78 eV) or the HCOOH pathway on the $*H_{1ML}$/Pd(111) surface over the hydrogenation to *HOCOH (E_a = 0.96 eV) or the HOCOH pathway and the dissociation to *CO or the rWGS pathway (E_a = 1.19 eV, Figure 3). In fact, even if *HOCO dissociates, the reverse reaction barrier is only 0.14eV due to the unstable co-adsorption of *CO and *OH on the $*H_{1ML}$/Pd(111) surface, and 98.2% of *CO and *OH is observed to convert back to *HOCO at 700 K and under 1 bar of CO_2 partial pressure. Similarly, 100% of formed *HOCOH is found to decompose back to *HOCO and *H, rather than *COH and *OH. This is not the case for the HCOOH pathway, where facile removal of produced *HCOOH (Table S1) greatly favors the *HOCO hydrogenation to *HCOOH going forward. Such selective catalytic performance has not been observed previously for metal catalysts including Pd(111). [27, 53]

The unique behavior of $*H_{1ML}$/Pd(111) is attributed to the Hv sites, which are generated during CO_2 hydrogenation and provide the active Pd sites underneath to interact with most of the reaction intermediates (Figure 2). It is constructed by removing one or two neighboring chemisorbed *H on $*H_{1ML}$/Pd(111), and is confined by the surrounding *H species on the surface. Such confined vacancy site is capable to accommodate the intermediates that requiring low symmetric sites, e.g. *HOCO and *HCOOH, but hindering the adsorption and the dissociative adsorption that requiring high symmetric sites, e.g. *HCOO, dissociation of *HOCO, *HCOOH and *HOCOH (Figure S3). In this way, the highly selective CO_2 hydrogenation to HCOOH is ensured on $*H_{1ML}$/Pd(111).

4. Conclusion

By combining DFT and KMC simulation, we identified the stable surface composition of Pd(111) under the typical CO_2 hydrogenation environment: Pd(111) fully covered by one monolayer of chemisorbed hydrogenation. More importantly, the hydrogen-covered Pd(111) was found behave differently from bare Pd(111), which favored the methanol synthesis according to the previous theoretical studies. The chemisorbed hydrogen on Pd(111) not only can act as hydrogen reservoir to facilitate the hydrogenation steps, but also can modify the binding to the reaction intermediates and reaction mechanism. Specifically, the hydrogenation generates the unique confined hydrogen vacancy sites on the surface, which are active to enable the effective selectivity-tuning to formic acid via the *HOCO intermediate and suppress the rWGS pathway to produce CO/water significantly. Yet the yield is highly dependent on temperature and mildly on partial pressure of CO_2 and H_2. Our study highlights the importance of description of catalytic behaviors under working conditions, where the reactive environment can result in the surface phase transformation and enable the variation in activity/selectivity.

Conflicts of interest

There are no conflicts to declare.

Acknowledgements

The research carried out at Brookhaven National Laboratory (BNL) was supported by the division of Chemical Science, Geoscience, and Bioscience, Office of Basic Energy Science of the US Department of Energy (DOE) under Contract No. DE-SC0012704. All the calculations in this work were performed using computational resources at Center for Functional

Nanomaterials (CFN), and the Scientific Data and Computing Center, a component of the Computational Science Initiative, at BNL under Contract No. DE-SC0012704, at the National Energy Research Scientific Computing Center (NERSC), a DOE Office of Science User Facility, supported by the Office of Science of the DOE under contract DE-AC02-05CH11231 and at Stony Brook University, which was founded by National Science Foundation grant (#1531492).

Notes and references

1. J. Artz, T. E. Muller, K. Thenert, J. Kleinekorte, R. Meys, A. Sternberg, A. Bardow and W. Leitner, *Chem. Rev.*, 2018, **118**, 434-504.
2. A. Saravanan, P. Senthil kumar, D.-V. N. Vo, S. Jeevanantham, V. Bhuvaneswari, V. Anantha Narayanan, P. R. Yaashikaa, S. Swetha and B. Reshma, *Chem. Eng. Sci.*, 2021, **236**, 116515.
3. X. Jiang, N. Koizumi, X. Guo and C. Song, *Appl. Catal. B: Environ.*, 2015, **170-171**, 173-185.
4. S. Das, J. Perez-Ramirez, J. Gong, N. Dewangan, K. Hidajat, B. C. Gates and S. Kawi, *Chem. Soc. Rev.*, 2020, **49**, 2937-3004.
5. W. L. Xiaowa Nie, Xiao Jiang Xinwen Guo, Chunshan Song, *Adv. Catal.*, 2019, **65**, 121-233.
6. X. Jiang, X. Nie, X. Guo, C. Song and J. G. Chen, *Chem. Rev.*, 2020, **120**, 7984-8034.
7. S. Dang, H. Yang, P. Gao, H. Wang, X. Li, W. Wei and Y. Sun, *Catal. Today*, 2019, **330**, 61-75.
8. R. Guil-Lopez, N. Mota, J. Llorente, E. Millan, B. Pawelec, J. L. G. Fierro and R. M. Navarro, *Materials (Basel)*, 2019, **12**, 3902.
9. W. Liao and P. Liu, *ACS Catal.*, 2020, **10**, 5723-5733.
10. X. Wang, P. J. Ramírez, W. Liao, J. A. Rodriguez and P. Liu, *J. Am. Chem. Soc.*, 2021, **143**, 13103-13112.
11. M. González-Castaño, B. Dorneanu and H. Arellano-García, *Reaction Chem. Eng.*, 2021, **6**, 954-976.
12. K. Oshima, T. Shinagawa, Y. Nogami, R. Manabe, S. Ogo and Y. Sekine, *Catal. Today*, 2014, **232**, 27-32.
13. M. Zhu, Q. Ge and X. Zhu, *Trans. Tianjin Univ.*, 2020, **26**, 172-187.
14. H. Zhang, X. Wang, A. I. Frenkel and P. Liu, *J. Chem. Phys.*, 2021, **154**, 014702.
15. Y. Kuwahara, Y. Fujie, T. Mihogi and H. Yamashita, *ACS Catal.*, 2020, **10**, 6356-6366.
16. Z. Zhang, L. Zhang, S. Yao, X. Song, W. Huang, M. J. Hülsey and N. Yan, *J. Catal.*, 2019, **376**, 57-67.
17. M. Li, Z. Sun and Y. H. Hu, *J. Mater. Chem. A*, 2021, **9**, 12495-12520.
18. S. Kattel, B. Yan, J. G. Chen and P. Liu, *J. Catal.*, 2016, **343**, 115-126.
19. O. A. Ojelade and S. F. Zaman, *Catal. Surv. Asia*, 2019, **24**, 11-37.
20. K. J. Betsy, A. Lazar, A. Pavithran and C. P. Vinod, *ACS Sustain. Chem. Eng.*, 2020, **8**, 14765-14774.
21. X. Wang, H. Shi, J. H. Kwak and J. Szanyi, *ACS Catal.*, 2015, **5**, 6337-6349.
22. H. Bahruji, M. Bowker, G. Hutchings, N. Dimitratos, P. Wells, E. Gibson, W. Jones, C. Brookes, D. Morgan and G. Lalev, *J. Catal.*, 2016, **343**, 133-146.
23. M. Zabilskiy, V. L. Sushkevich, M. A. Newton, F. Krumeich, M. Nachtegaal and J. A. van Bokhoven, *Angew. Chem. Int. Ed.*, 2021, **60**, 17053-17059.
24. N. Rui, Z. Y. Wang, K. H. Sun, J. Y. Ye, Q. F. Ge and C. J. Liu, *Appl. Catal. B-Environ.*, 2017, **218**, 488-497.
25. S. E. Collins, D. L. Chiavassa, A. L. Bonivardi and M. A. Baltanás, *Catal. Lett.*, 2005, **103**, 83-88.
26. I. Melian Cabrera, *J. Catal.*, 2002, **210**, 285-294.
27. F. Brix, V. Desbuis, L. Piccolo and E. Gaudry, *J. Phys. Chem. Lett.*, 2020, **11**, 7672-7678.
28. M. Zhang, Y. Wu, M. Dou and Y. Yu, *Catal. Letters*, 2018, **148**, 2935-2944.
29. A. G. Saputro, A. L. Maulana, F. Fathurrahman, G. Shukri, M. H. Mahyuddin, M. K. Agusta, T. D. K. Wungu and H. K. Dipojono, *Int. J. Hydrogen Energy*, 2021, **46**, 14418-14428.
30. A. G. Saputro, R. I. D. Putra, A. L. Maulana, M. U. Karami, M. R. Pradana, M. K. Agusta, H. K. Dipojono and H. Kasai, *J. Energy Chem.*, 2019, **35**, 79-87.
31. D. Gao, H. Zhou, F. Cai, D. Wang, Y. Hu, B. Jiang, W.-B. Cai, X. Chen, R. Si, F. Yang, S. Miao, J. Wang, G. Wang and X. Bao, *Nano Res.*, 2017, **10**, 2181-2191.
32. W. Sheng, S. Kattel, S. Yao, B. Yan, Z. Liang, C. J. Hawxhurst, Q. Wu and J. G. Chen, *Energy Environ. Sci.*, 2017, **10**, 1180-1185.
33. J. P. Simonovis, H. Zhang, N. Rui, A. Hunt, I. Orozco, P. Liu, S. D. Senanayake, J. A. Rodriguez and I. Waluyo, *The J. Phys. Chem. C*, 2022, **126**, 7870-7879.
34. G. Kresse and J. Furthmüller, *Phys. Rev. B Condens. Matter*, 1996, **54**, 11169-11186.
35. G. Kresse and D. Joubert, *Phys. Rev. B*, 1999, **59**, 1758-1775.
36. G. Kresse and J. Furthmüller, *Comput. Mater. Sci.*, 1996, **6**, 15-50.
37. J. P. Perdew, K. Burke and M. Ernzerhof, *Phys. Rev. Lett.*, 1996, **77**, 3865-3868.
38. V. Wang, N. Xu, J.-C. Liu, G. Tang and W.-T. Geng, *arXiv:1908.08269*, 2019.
39. R. Peköz and D. Donadio, *J. Chem. Phys.*, 2016, **145**, 104701.
40. W. H. Press, B. P. Flannery, S. A. Teukolsky and W. T. Vetterling, *Numerical Recipes: The Art of Scientific Computing*, Cambridge University Press, New York, 1986.
41. P. Pulay, *Chem. Phys. Lett.*, 1980, **73**, 393-398.
42. G. Mills, H. Jónsson and G. K. Schenter, *Surf. Sci.*, 1995, **324**, 305-337.
43. H. Jónsson, G. Mills, K. W. Jacobsen, Nudged elastic band method for finding minimum energy paths oftransitions in *Classical and Quantum Dynamics in Condensed Phase Simulations*, World Scientific, 1998, 385-404.
44. G. Henkelman and H. Jónsson, *J. Chem. Phys.*, 2000, **113**, 9978-9985.
45. G. Henkelman, B. P. Uberuaga and H. Jónsson, *J. Chem. Phys.*, 2000, **113**, 9901-9904.
46. E. Bitzek, P. Koskinen, F. Gahler, M. Moseler and P. Gumbsch, *Phys. Rev. Lett.*, 2006, **97**, 170201.
47. P. Pulay, *Chem. Phys. Lett.*, 1980, **73**, 393-398.
48. R. A. v. S. H. J. W. Niemantsverdriet, *Chemical Kinetics and Catalysis (Fundamental and Applied Catalysis)*, Plenum Press, New York, 1995.
49. NIST Computational Chemistry Comparison and Benchmark DataBase, NIST Standard Reference Database

Number 101, Release 22, May 2022, Editor: Russell D. Johnson III, http://cccbdb.nist.gov/.
50. M. Chase, NIST-JANAF Thermochemical Tables 2 Volume-Set (Journal of Physical and Chemical Reference Data Monographs), *American Institute of Physics*, 1998.
51. J. Scaranto and M. Mavrikakis, *Surf. Sci.*, 2016, **650**, 111-120.
52. M. Liu, Y. H. Yi, L. Wang, H. C. Guo and A. Bogaerts, *Catalysts*, 2019, **9**, 275.
53. P. Liu, Y. Yang and M. G. White, in *Surf. Sci. Rep.* 2013, **68**, 233-272.